RSC Advances

PAPER

View Article Online
View Journal | View Issue

Cite this: *RSC Adv.*, 2021, **11**, 12442

Prominent roles of $Ni(OH)_2$ deposited on $ZnIn_2S_4$ microspheres in efficient charge separation and photocatalytic H_2 evolution†

Zhuang Guo, Huixia Hou, Jingyi Zhang, Pinglong Cai and Jun Lin *

Received 2nd March 2021
Accepted 23rd March 2021

DOI: 10.1039/d1ra01648b

rsc.li/rsc-advances

In this work, $Ni(OH)_2$-deposited $ZnIn_2S_4$ microspheres ($Ni(OH)_2/ZnIn_2S_4$) were fabricated using a hydrothermal process, followed by a facile *in situ* precipitation method. It was demonstrated that the deposition of $Ni(OH)_2$ on $ZnIn_2S_4$ effectively promotes the separation of charges photogenerated over $ZnIn_2S_4$, and significantly enhances photocatalytic H_2 evolution. The optimum rate of the photocatalytic H_2 evolution over the 6% $Ni(OH)_2/ZnIn_2S_4$ composite reaches 4.43 mmol g^{-1} h^{-1}, which is 21.1 times higher than that of the pure $ZnIn_2S_4$. Based on various characterization results and Au photo-deposition on the composite, it was proposed that the capture of the photogenerated holes by the deposited $Ni(OH)_2$ would be responsible for the efficient charge separation, which allows more photogenerated electrons to be left on the $ZnIn_2S_4$ for the reduction of H^+ to H_2 with a higher rate.

1. Introduction

Photocatalytic hydrogen production by water splitting has become one of the sustainable and environmentally friendly strategies for solving the consumption of fossil fuels and the resulting environmental pollution.[1–3] For the full utilization of solar energy, a considerable number of narrow band gap semiconductors have been widely investigated as visible light photocatalysts for hydrogen production. Of these semiconductors, CdS, g-C_3N_4, and $ZnIn_2S_4$ have received intensive attention since their band gaps match well with the spectrum of sunlight, and their conduction band edges are more negative than the redox potential of H^+/H_2.[4–6] Unfortunately, the direct application of these semiconductors themselves for photocatalytic H_2 production is almost infeasible mainly due to their rapid charge recombination.[7–9] For an efficient photocatalytic H_2 production reaction, it is indispensable to load a noble metal such as Pt, Pd, Ag, or Au as a cocatalyst on the host semiconductors.[10–13] The noble metals as cocatalysts can not only facilitate the separation of electron–hole pairs over host semiconductor effectively, but also function as active sites for H_2 production. Nevertheless, the high cost and scarcity of these noble metals seriously hinder their practical application. Therefore, it is desirable to exploit noble metal-free, abundant, and durable cocatalysts for photocatalytic H_2 production.

Recently, numerous works reported that the modification of various narrow band gap semiconductors with molybdenum disulfide (MoS_2), an earth-abundant compound, significantly enhances photocatalytic H_2 production from water splitting and quantum efficiency.[14–16] Both experimental and computational results also well revealed the photogenerated charge transfer, capture, and active sites for H_2 production in the systems with MoS_2 as a cocatalyst.[17,18] Afterward, other transition metal (*e.g.* Ni, Co, Cu, Fe) disulfides and phosphides have been investigated and utilized as cocatalysts for assisting photocatalytic H_2 production.[19–22] In addition, hydroxide can also act as a cocatalyst for photocatalytic H_2 production. In 2011, a typical pioneer work reported that $Ni(OH)_2$-decorated TiO_2 could give a H_2 evolution rate of 3056 μmol g^{-1} h^{-1} and a quantum efficiency of 12.4% under UV irradiation, which is 233 times than that of pure TiO_2.[23] Following this work, hydroxides such as $Ni(OH)_2$ and $Co(OH)_2$ have been widely applied as cocatalysts for photocatalytic H_2 production by coupling with proper narrow band gap semiconductors including CdS, g-C_3N_4, and $ZnIn_2S_4$.[24–29] These works have well demonstrated that the hydroxides are capable of being alternatives for noble metal cocatalysts, and deserve more and further attention in photocatalytic H_2 production. Especially, the deepening of the knowledge of photogenerated charge transfer, capture, and active sites for H_2 production would be helpful for the design and optimization of hydroxide-modified photocatalysts. In the present work, we fabricated the $Ni(OH)_2$-deposited $ZnIn_2S_4$ composites by a facile *in situ* precipitation method. Upon visible light irradiation, the photocatalytic activity of $ZnIn_2S_4$ for H_2 evolution has been shown to be significantly enhanced after the deposition of $Ni(OH)_2$. Furthermore, the roles of the deposited $Ni(OH)_2$ in the enhanced photocatalytic H_2 evolution of the composite were

Department of Chemistry, Renmin University of China, Beijing 100872, People's Republic of China. E-mail: jlin@ruc.edu.cn; Fax: +8610-62516444; Tel: +8610-62514133

† Electronic supplementary information (ESI) available. See DOI: 10.1039/d1ra01648b

revealed according to various characterization results and photodeposition of Au nanoparticles on the composite. This work, we believe, offers a new insight into the photogenerated charge capture, separation, and active sites for H_2 evolution in the composite.

2. Experimental section

2.1. Sample preparation

$ZnIn_2S_4$ samples were synthesized by a literature method with a slight modification.[30] Briefly, 0.2862 g of $ZnCl_2$ and 1.2484 g of $InCl_3 \cdot 4H_2O$ were dissolved in 40 ml of distilled water under vigorous stirring, followed by the addition of polyethylene glycol (PEG-6000, 0.8836 g) and thioacetamide (TAA, 1.2096 g). The obtained mixture, a homogeneous solution, was transferred into a 100 ml Teflon-lined stainless steel autoclave and heated at 160 °C for 16 h in an oven. After cooled down to room temperature naturally, the yellow products $ZnIn_2S_4$ were collected by centrifugation and washed with water and ethanol for three times before dried at 60 °C in a vacuum oven for overnight.

The deposition of $Ni(OH)_2$ on the surface of $ZnIn_2S_4$ was conducted by a facile *in situ* precipitation method. In a typical procedure, 0.2 g of the as-prepared $ZnIn_2S_4$ was dispersed in 50 ml of NaOH aqueous solution (0.25 M). Under agitation, into the dispersion was the desired amount of $Ni(NO_3)_2 \cdot 6H_2O$ aqueous solution (0.05 M) added dropwise. The resulting mixture was stirred for 5 h at room temperature. Subsequently, the final product was collected by centrifugation, and thoroughly washed with deionized water, and finally dried in a vacuum oven at 60 °C for 12 h. According to the nominal molar ratios of $Ni(NO_3)_2$ to ($Ni(NO_3)_2$ + $ZnIn_2S_4$) in the above procedure, the obtained samples were denoted as 0%, 2%, 4%, 6%, and 8% $Ni(OH)_2/ZnIn_2S_4$, respectively.

2.2. Characterization

The polycrystalline X-ray diffraction (XRD) patterns of the prepared samples were collected on an X-ray diffractometer (Shimadzu, XRD-7000) with Cu Kα radiation under 40 kV and 150 mA. The morphological and microstructural features of the samples were captured by using a field-emission scanning microscope (FESEM) (JEOL 6701F) and a high-resolution transmission electron microscope (HRTEM) (JEOL-2010), respectively. X-ray photoelectron spectroscopy (XPS) analysis was performed in a Thermo ESCALAB 250 electron spectrometer with a monochromatic Al Kα source. All the binding energies were referenced to the C 1s peak of the surface adventitious carbon at 284.6 eV. The optical absorption properties of the samples were analyzed with UV-visible diffuse reflectance spectroscopy (Hitachi UH-4150) with $BaSO_4$ as a reflectance standard.

Transient photocurrent response and electrochemical impedance spectroscopy (EIS) measurements were carried out in a three-electrode system on an electrochemical work station (Chenhua, Shanghai). A Pt wire and a Ag/AgCl in a saturated KCl solution were employed as the counter electrode and the reference electrode, respectively. The working electrode was prepared by coating sample slurry onto ITO glass substrate with a fixed area of 1 × 1 cm^2 followed by drying with an infrared lamp irradiation. A 1.0 M Na_2SO_4 aqueous solution was used as the electrolyte for both photocurrent response and electrochemical impedance spectroscopy (EIS) measurements. The visible light irradiation source is a 3 W monochromatic light (λ = 420 nm).

2.3. Photocatalytic experiments

The experiments of the photocatalytic H_2 production over these prepared samples irradiated by visible light were carried out in a gas-closed Pyrex flask at ambient temperature. Typically, 20 mg of the prepared sample powder was suspended in 100 ml of 10 vol% lactic acid aqueous solution under magnetic stirring. The suspension was thoroughly degassed with N_2 for 30 min before irradiated by a 300 W Xe arc lamp (LabSolar II, Perfect Light Co., Ltd) equipped with a cut-off filter (λ > 420 nm). The amount of hydrogen evolution during the reaction was periodically analyzed by a gas chromatography (GC-2014C, Shimadzu, Japan) with a TCD detector and a molecular sieve 5A column with N_2 as the carrier gas.

To study the reduction sites for H_2 evolution in the $Ni(OH)_2/ZnIn_2S_4$ composite, the photocatalytic deposition of Au on 6% $Ni(OH)_2/ZnIn_2S_4$ was performed at ambient temperature. Briefly, 50 mg of 6% $Ni(OH)_2/ZnIn_2S_4$ composite was dispersed in 50 ml of 10 vol% benzyl alcohol aqueous solution under stirring, followed by the addition of 52 μl of $HAuCl_4 \cdot 4H_2O$ aqueous solution (1 g/50 ml). Prior to the irradiation by a 300 W Xe arc lamp (LabSolar II, Perfect Light Co., Ltd) equipped with a cut-off filter (λ > 420 nm), the dispersion was thoroughly degassed with N_2 for 30 min. After the irradiation for 2 h, the composite was collected by centrifugation, washed with ethanol and water several times, and finally dried at 60 °C in a vacuum oven overnight for further TEM observation.

3. Results and discussion

3.1. Phase structure and morphology

The polycrystalline X-ray diffraction patterns of the prepared pure $ZnIn_2S_4$ and $Ni(OH)_2/ZnIn_2S_4$ composites are shown in

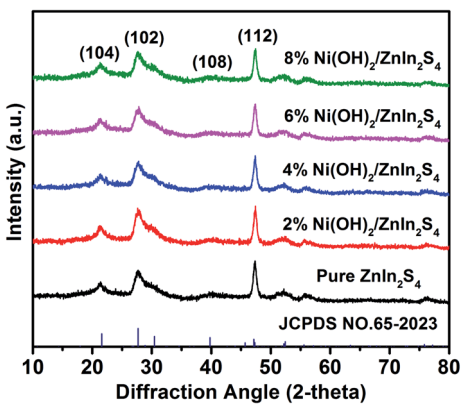

Fig. 1 Polycrystalline X-ray diffraction patterns of pure $ZnIn_2S_4$ and $Ni(OH)_2/ZnIn_2S_4$ composites.

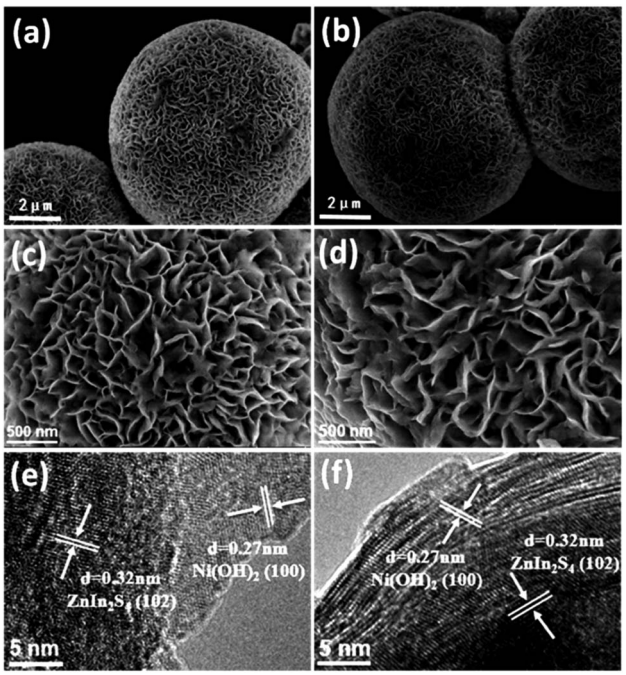

Fig. 2 FESEM images of (a and c) pure $ZnIn_2S_4$ and (b and d) 6% $Ni(OH)_2/ZnIn_2S_4$ with different scales; (e and f) HRTEM images of 6% $Ni(OH)_2/ZnIn_2S_4$.

Fig. 1. All samples exhibit a single characteristic hexagonal phase of $ZnIn_2S_4$ (JPCDS no. 65-2023), and no changes in the intensities and widths of the XDR peaks occur with the $Ni(OH)_2$ loading. These indicate that the deposition of $Ni(OH)_2$ on $ZnIn_2S_4$ doesn't alter the phase structure and crystallinity of $ZnIn_2S_4$ substrate. Notably, the relative intensity of (112) diffraction peak at approximately 47.5 degree for all samples is obviously enhanced as compared to the corresponding one of the reference (JPCDS no. 65-2023). This is perhaps due to the preferential orientation growth of the crystalline plane (112) in our synthesis process. Moreover, no characteristic XRD peaks associated with $Ni(OH)_2$ are observed in all $Ni(OH)_2/ZnIn_2S_4$ composites, which is probably due to the low content and high dispersion of $Ni(OH)_2$ on $ZnIn_2S_4$. The presence of $Ni(OH)_2$ would be confirmed by the HRTEM observation and XPS analysis below.

Fig. 2a and b display the FESEM images of the pure $ZnIn_2S_4$ and 6% $Ni(OH)_2/ZnIn_2S_4$ composite, respectively. As can be seen in Fig. 2a, the pure $ZnIn_2S_4$ shows uniform microspheres with an average diameter of *ca.* 6–8 μm. These microspheres (Fig. 2c) consist of a great number of curling nanosheets, which could be helpful for the deposition of $Ni(OH)_2$ and photocatalytic H_2 evolution by offering a large surface area. A careful observation (Fig. 2b and d) indicates that the introduction of $Ni(OH)_2$ doesn't alert the morphology and size of $ZnIn_2S_4$ microsphere, except that the curling nanosheets become a little rough. The HRTEM images (Fig. 2e and f) of 6% $Ni(OH)_2/ZnIn_2S_4$ composite reveals that the crystalline $Ni(OH)_2$ are well deposited onto the surface of well-crystalline $ZnIn_2S_4$ to form heterostructures with the intimate interfaces.[7,8] The lattice fringes with the spacing of *ca.* 0.32 nm and 0.27 nm well correspond to the crystallographic plane (102) of hexagonal $ZnIn_2S_4$ and the crystallographic plane (100) of hexagonal $Ni(OH)_2$,

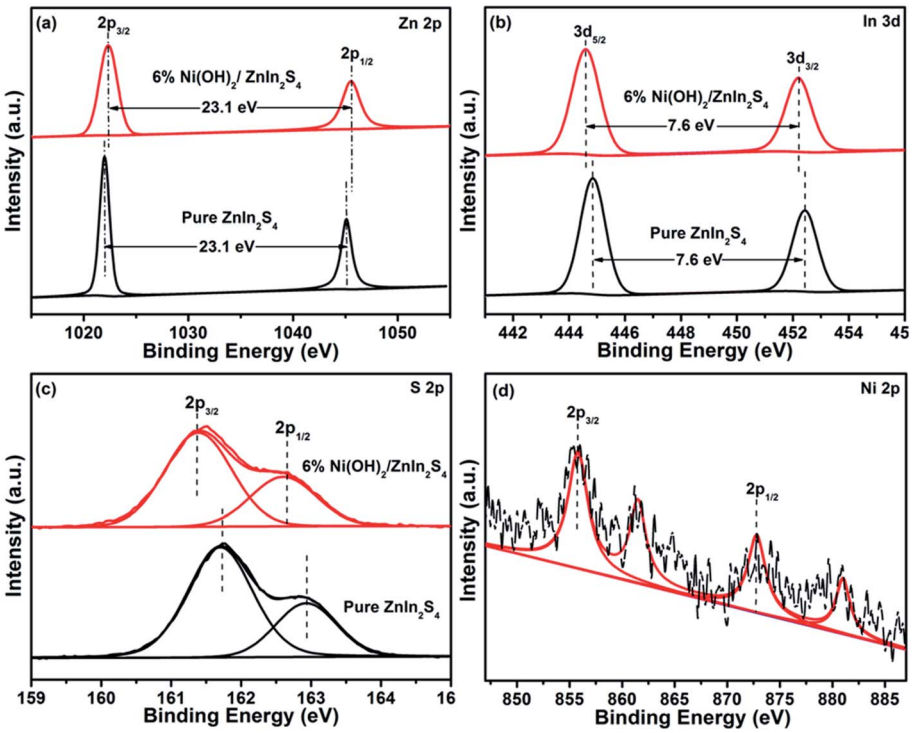

Fig. 3 High resolution XPS spectra of Zn 2p (a), In 3d (b), and S 2p (c) in pure $ZnIn_2S_4$ and 6% $Ni(OH)_2/ZnIn_2S_4$, and Ni 2p (d) in 6% $Ni(OH)_2/ZnIn_2S_4$.

respectively.[25,31] The high-angle annular dark field-scanning transmission electron microscopy (HAADF-STEM) image (Fig. S1a†) and energy dispersive spectroscopy (EDS) elemental mapping (Fig. S1b–f†) analysis of 6% $Ni(OH)_2/ZnIn_2S_4$ composite was performed to characterize the elemental constitute and distribution. The elemental mapping confirms the uniform distribution of Zn, In, S, Ni, and O elements over the selected detection area of the composite. The weaker signals of Ni and O are well consistent with the lower molar percentage of $Ni(OH)_2$ in the composite.

3.2. XPS analysis and optical property

The compositions and chemical states of the elements in the pure $ZnIn_2S_4$ and 6% $Ni(OH)_2/ZnIn_2S_4$ were further analyzed by XPS. The XPS survey spectra, as displayed in Fig. S2,† clearly indicate the presence of Zn, In, S, O, and C in both samples, and Ni in 6% $Ni(OH)_2/ZnIn_2S_4$ only. Fig. 3a–c show the high resolution spectra of Zn 2p, In 3d, and S 2p regions of the pure $ZnIn_2S_4$ and 6% $Ni(OH)_2/ZnIn_2S_4$, respectively. In the Zn 2p core-level spectrum of pure $ZnIn_2S_4$ (Fig. 3a), two peaks at the binding energies of 1021.9 and 1045.0 eV, with a separation of 23.1 eV, are assigned to Zn $2p_{3/2}$ and Zn $2p_{1/2}$ of Zn^{2+}, respectively.[32] The two symmetric peaks of In 3d located at the binding energies of 444.8 and 452.4 eV in the In 3d core-level spectrum of pure $ZnIn_2S_4$ with a peak difference of 7.6 eV (Fig. 3b) are ascribed to In $3d_{5/2}$ and In $3d_{3/2}$ of In^{3+}, respectively.[33,34] The S 2p spectrum of pure $ZnIn_2S_4$ shown in Fig. 3c appears to be a broad peak, which can be deconvoluted two peaks with the binding energies of 161.7 and 162.9 eV, corresponding to S $2p_{3/2}$ and S $2p_{1/2}$, respectively.[31,35] Collectively, the binding energies of Zn, In, and S match well the feature of $ZnIn_2S_4$. The high resolution XPS spectrum of Ni 2p, as shown in Fig. 3d, clearly demonstrates two main peaks at 855.7 and 873.1 eV corresponding to typical Ni $2p_{3/2}$ and Ni $2p_{1/2}$, respectively.[25] Two shake-up satellite peaks for Ni $2p_{3/2}$ and Ni $2p_{1/2}$ are observed at 861.5 and 880.8 eV. These binding energies of Ni 2p indicate the characteristic of Ni^{2+} in $Ni(OH)_2$ based on the literature reports.[36] It is worth noting that the deposition of $Ni(OH)_2$ on $ZnIn_2S_4$ cause a slight shift in the binding energies of Zn 2p, In 3d, and S 2p peaks. The observed shifts suggest a strong chemical bond between $Ni(OH)_2$ and $ZnIn_2S_4$, which would be favorable for the charge transfer between them. The XPS measurements evidence the formation of $Ni(OH)_2$-deposited $ZnIn_2S_4$ heterostructures with the well-contacted interfaces, further confirming the above HRTEM observation.

The optical absorption properties of the pure $ZnIn_2S_4$ and $Ni(OH)_2/ZnIn_2S_4$ composites with the different amount of deposited $Ni(OH)_2$ were investigated by UV-visible diffuse reflectance spectroscopy. As displayed in Fig. 4, the pure $ZnIn_2S_4$ exhibits an intense absorption with an edge at *ca.* 525 nm, which can be attributed to the intrinsic band gap absorption of hexagonal $ZnIn_2S_4$ (~2.36 eV). This coincides with the reported value of $ZnIn_2S_4$.[37] In contrast with the pure $ZnIn_2S_4$, the deposition of $Ni(OH)_2$ enhances the light absorption in the visible region. The absorption intensity of the composites in visible region gradually increases with the increase of the molar ratio of $Ni(OH)_2$ in the composites. Furthermore, almost no obvious absorption edge differences among the absorption spectra of the pure $ZnIn_2S_4$ and $Ni(OH)_2/ZnIn_2S_4$ composites suggest the deposition of $Ni(OH)_2$ on the surface of $ZnIn_2S_4$.

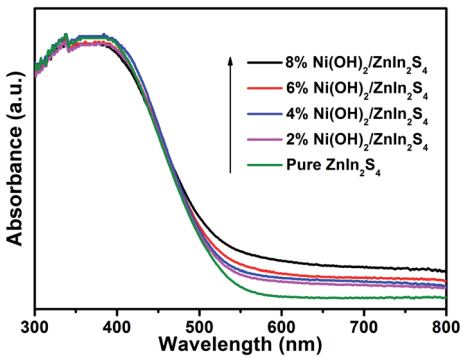

Fig. 4 UV-vis diffuse reflectance spectra of pure $ZnIn_2S_4$ and $Ni(OH)_2/ZnIn_2S_4$ composites.

3.3. Photocatalytic H_2 evolution

The photocatalytic H_2 evolution over the pure $ZnIn_2S_4$, $Ni(OH)_2$, and $Ni(OH)_2/ZnIn_2S_4$ composites was evaluated under visible light (λ > 420 nm) irradiation in the presence of lactic acid as a sacrificial reagent. Control experiments show that no appreciable H_2 evolution is detected in the absence of either visible light irradiation or catalyst. As depicted in Fig. 5a, H_2 evolution rate over the pure $ZnIn_2S_4$ is negligible due to the rapid recombination of electron–hole pairs over the irradiated pure $ZnIn_2S_4$, and also no appreciable H_2 activity is observed on pure $Ni(OH)_2$. However, a proper combination of both generates excellent photocatalytic H_2 evolution. As the deposition of 2% $Ni(OH)_2$ on $ZnIn_2S_4$, the rate of H_2 evolution is significantly enhanced to 2.20 mmol g^{-1} h^{-1}. The rate of H_2 evolution further increases with the amount of deposited $Ni(OH)_2$, and reaches an optimum of 4.43 mmol g^{-1} h^{-1} over 6% $Ni(OH)_2/ZnIn_2S_4$, which is 21.2 times higher than that of pure $ZnIn_2S_4$. After the optimum, the reduction in H_2 evolution rate over 8% $Ni(OH)_2/ZnIn_2S_4$ would be attributed to the shielding effect of excessive $Ni(OH)_2$ which impedes the light absorption of the substrate $ZnIn_2S_4$. The above result well demonstrates the deposition of $Ni(OH)_2$ with an appropriate amount is an effective method for boosting the photocatalytic H_2 evolution over $ZnIn_2S_4$, which is consistent with the related literatures.[25]

The stability of photocatalytic H_2 evolution over 6% $Ni(OH)_2/ZnIn_2S_4$ was examined by conducting the photocatalytic recycle experiments. As shown in Fig. 5b, after three recycle (12 h), no apparent decrease in H_2 evolution over the composite can be observed, indicating the good stability of the composite for photocatalytic H_2 evolution.

3.4. Mechanism of enhanced photocatalytic H_2 evolution over $Ni(OH)_2/ZnIn_2S_4$

To understand the mechanism of the enhanced photocatalytic H_2 evolution over $Ni(OH)_2/ZnIn_2S_4$, the role of the deposited

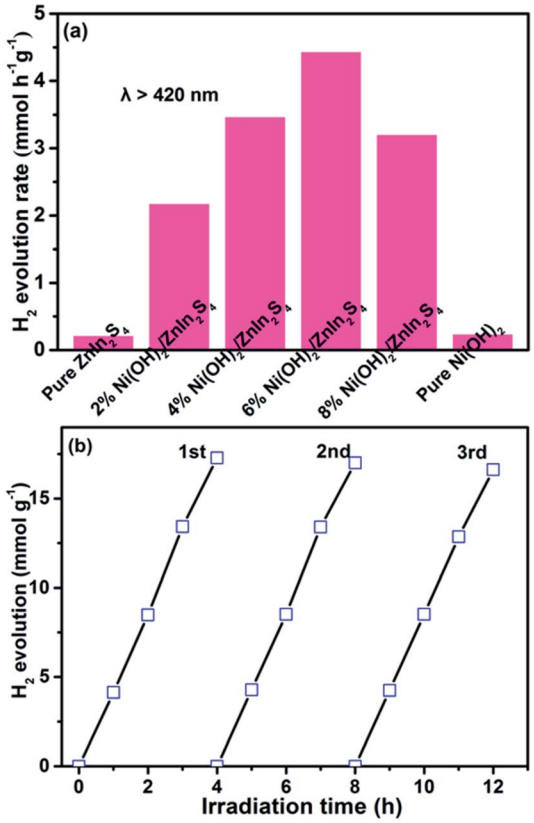

Fig. 5 (a) Photocatalytic H_2 evolution rates over pure $ZnIn_2S_4$, $Ni(OH)_2$, and $Ni(OH)_2/ZnIn_2S_4$ composites. (b) Cycling photocatalytic H_2 evolution over 6% $Ni(OH)_2/ZnIn_2S_4$.

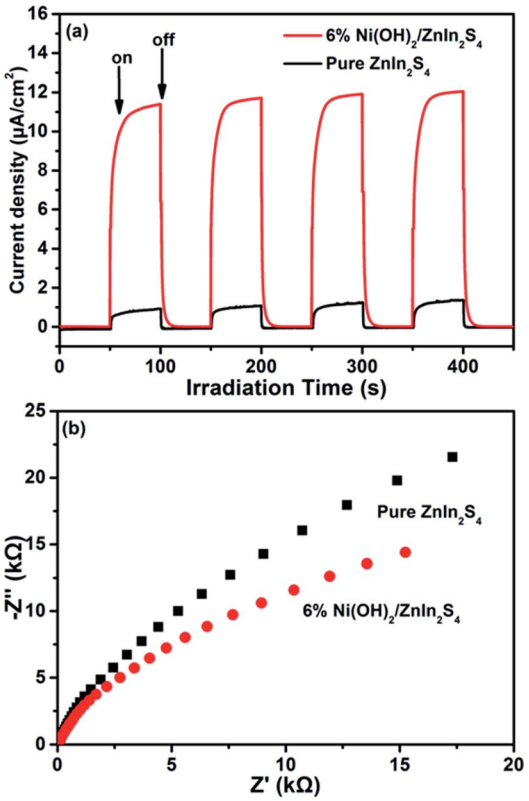

Fig. 6 Transient photocurrent responses (a) and electrochemical impedance spectroscopy Nyquist plots (b) of pure $ZnIn_2S_4$ and 6% $Ni(OH)_2/ZnIn_2S_4$.

$Ni(OH)_2$ on the surface of $ZnIn_2S_4$ in the transfer and separation of charges photogenerated over $ZnIn_2S_4$ was investigated by measuring the transient photocurrent response. Fig. 6a shows the transient photocurrent responses of the pure $ZnIn_2S_4$ and 6% $Ni(OH)_2/ZnIn_2S_4$ under visible light irradiation ($\lambda = 420$ nm) with 50 s light on/off cycles. It can be clearly observed that 6% $Ni(OH)_2/ZnIn_2S_4$ exhibits much higher photocurrent density than pure $ZnIn_2S_4$. As well known, the photocurrent density is directly proportional to the transfer and separation of photogenerated charge.[38,39] The higher photocurrent density over 6% $Ni(OH)_2/ZnIn_2S_4$ composite than pure $Ni(OH)_2$ reveals that the deposition of $Ni(OH)_2$ on $ZnIn_2S_4$ benefits the charge transfer across the intimate interfaces between $Ni(OH)_2$ and $ZnIn_2S_4$, and achieves the efficient separation of charges photogenerated over $ZnIn_2S_4$. Moreover, the interfacial charge transfer and separation of two samples was also characterized by electrochemical impedance spectroscopy (EIS) measurements, as shown in Fig. 6b. Generally, the small curvature radius of the Nyquist curves represents a low charge transfer resistance, suggesting the efficient separation and transfer of photogenerated charges. The smaller curvature radius of the EIS plot of 6% $Ni(OH)_2/ZnIn_2S_4$ compared to that of pure $ZnIn_2S_4$ further confirms that the efficient separation and transfer of photogenerated charges are realized after the introduction of $Ni(OH)_2$.[40] The transient photocurrent response and electrochemical impedance spectroscopy (EIS) results of two samples parallel their performances (Fig. 5a) for photocatalytic H_2 evolution.

Based on the above results of the transient photocurrent response and electrochemical impedance spectroscopy measurements, without a doubt, it is the deposition of $Ni(OH)_2$ on the surface of $ZnIn_2S_4$ that the efficient separation of electron–hole pairs photogenerated over $ZnIn_2S_4$ has been achieved through the charge transfer across the intimate interfaces between $Ni(OH)_2$ and $ZnIn_2S_4$. Subsequently, we need to elucidate how the deposited $Ni(OH)_2$ effectively promotes the charge transfer to realize the separation of electron–hole pairs. According to the literature reports, the conduction band (CB) and valence band (VB) edges of $ZnIn_2S_4$ are −1.35 V and +1.4 V *vs.* NHE, respectively,[31] while the redox potentials of $Ni(OH)_2/Ni$ and $Ni(OH)_3/Ni(OH)_2$ are −0.72 V and +0.48 *vs.* NHE, respectively.[41] From the view of thermodynamics, thus, there are two possible paths that the deposited $Ni(OH)_2$ promotes the separation of electron–hole pairs photogenerated over $ZnIn_2S_4$ composite. In path I, the photo-induced electrons on CB of $ZnIn_2S_4$ transfer to the deposited $Ni(OH)_2$ and reduce partial Ni^{2+} to form Ni^0, where the bound proton H^+ accepts the electrons from Ni^0 to be reduced to H_2. In path II, the photo-induced holes on VB of $ZnIn_2S_4$ are scavenged by the deposited $Ni(OH)_2$ to form $Ni(OH)_3$, allowing the electrons left on CB of $ZnIn_2S_4$ to reduce H^+ to H_2. Obviously, the reduction sites of

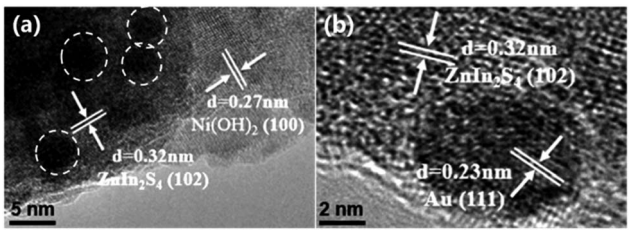

Fig. 7 TEM (a) and HRTEM (b) images of Au-photodeposited 6% $Ni(OH)_2/ZnIn_2S_4$.

H^+ to H_2 in two paths are on the deposited $Ni(OH)_2$ and $ZnIn_2S_4$, respectively. Either path I or path II is an actual running one. This problem, we believe, can be clarified by the identification of the reduction sites in $Ni(OH)_2/ZnIn_2S_4$ composite. To this end, the photocatalytic deposition of Au on 6% $Ni(OH)_2/ZnIn_2S_4$ composite was conducted in the presence of $HAuCl_4 \cdot 4H_2O$ as Au precursor. As shown in Fig. 7a, after the photo-deposition of Au on the composite, several dark gray nanoparticles clearly appear on the surface of the crystalline $ZnIn_2S_4$ only.[7,8] A HRTEM (Fig. 7b) analysis further indicates that the lattice fringe of 0.23 nm in a dark gray nanoparticle matches the crystallographic plane (111) of metallic cubic-phase Au.[42] The results well demonstrate that the reduction of $AuCl_4^-$ to Au^0 by the photogenerated electrons in the composite occurs on the surface of $ZnIn_2S_4$ rather than $Ni(OH)_2$, suggesting that the photogenerated electrons are left on the $ZnIn_2S_4$, not transferred to the $Ni(OH)_2$. In the same way, the sites for the reduction of H^+ to H_2 in $Ni(OH)_2/ZnIn_2S_4$ composite should be also on the surface of $ZnIn_2S_4$, which excludes the possibility of path I.

According to the above discussion and various experiments, therefore, a understanding of the enhanced photocatalytic H_2 evolution over $Ni(OH)_2/ZnIn_2S_4$ composite can be schematically illustrated in Scheme 1. The H_2 evolution rate is very low over the pure $ZnIn_2S_4$ due to the rapid recombination of CB electrons and VB holes. After the deposition of $Ni(OH)_2$ on $ZnIn_2S_4$, the VB holes can be scavenged by deposited $Ni(OH)_2$ to form $Ni(OH)_3$ across the intimate interfaces between $ZnIn_2S_4$ and $Ni(OH)_2$ since the valence band edge of $ZnIn_2S_4$ (+1.4 V *vs.* NHE) is more positive than the redox potential of $Ni(OH)_3/Ni(OH)_2$ (+0.48 *vs.* NHE).[41] This leads to an efficient separation of charges photogenerated over $ZnIn_2S_4$ and allows more photogenerated electrons left on the surface of $ZnIn_2S_4$ to reduce the bound protons H^+ to H_2, enhancing photocatalytic activity. Meanwhile, the formed $Ni(OH)_3$ can easily become back to $Ni(OH)_2$ through the oxidation of the added lactic acid as a sacrificial reagent, continuously driving the charge separation.

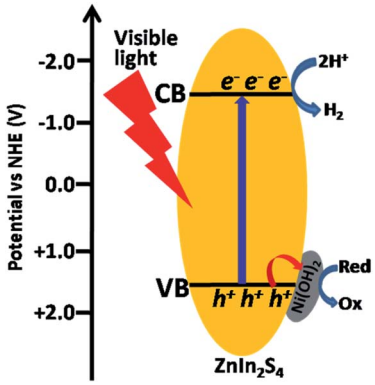

Scheme 1 Schematic illustration of photocatalytic H_2 evolution over $Ni(OH)_2/ZnIn_2S_4$ composite.

4. Conclusion

In summary, the crystalline $Ni(OH)_2$ have been successfully deposited on the surface of $ZnIn_2S_4$ through a facile *in situ* precipitation method. The deposition of $Ni(OH)_2$ on $ZnIn_2S_4$ was demonstrated to significantly enhance the photocatalytic H_2 evolution over $ZnIn_2S_4$. Various characterization results indicate that the deposition of $Ni(OH)_2$ on $ZnIn_2S_4$ effectively promotes the separation of charges photogenerated over $ZnIn_2S_4$. Furthermore, the experiment of the photodeposition of Au nanoparticles reveals that the scavenging of the photogenerated holes by the deposited $Ni(OH)_2$ effectively inhibits the recombination rate of the electron–hole pairs, boosting a high photocatalytic H_2 evolution rate over $ZnIn_2S_4$.

Author contributions

Zhuang Guo synthesized samples, conducted various characterizations, and drafted the paper. Huixia Hou, Jingyi Zhang and Pinglong Cai performed the electrochemical measurements and participated in the photocatalytic experiments. Jun Lin conceived the idea, revised the paper, and approved the final version.

Conflicts of interest

There are no conflicts to declare.

Acknowledgements

This work was financially supported by the National Natural Science Foundation of China (Grant No. 21673287).

Notes and references

1 A. Kudo and Y. Miseki, *Chem. Soc. Rev.*, 2009, **38**, 253–278.
2 U. Maitra, U. Gupta, M. De, R. Datta, A. Govindaraj and C. Rao, *Angew. Chem., Int. Ed.*, 2013, **52**, 13057–13061.
3 Y. X. Fang, X. C. Li and X. C. Wang, *ACS Catal.*, 2018, **8**, 8774–8780.
4 X. Yan, Z. L. Jin, Y. P. Zhang, H. Liu and X. L. Ma, *Phys. Chem. Chem. Phys.*, 2019, **21**, 4501–4512.
5 H. Wei, W. A. McMaster, J. Z. Y. Tan, L. Cao, D. Chen and R. A. Caruso, *J. Phys. Chem. C*, 2017, **121**, 22114–22122.
6 Z. Guan, Z. Xu, Q. Li, P. Wang, G. Li and J. Yang, *Appl. Catal., B*, 2018, **227**, 512–518.
7 A. Luna-Flores, M. A. Morales, R. Agustín-Serrano, R. Portillo, J. A. Luna-López, G. F. Pérez-Sánchez, A. D. Hernández-de la Luz and N. Tepale, *Catalysts*, 2019, **9**, 817.

8 M. A. Moralesa, I. Fernández-Cervantesb, R. Agustín-Serranoe, S. Ruíz-Salgadoa, M. P. Sampedroa, J. L. Varela-Caselisc, R. Portillod and E. Rubio, *Results Phys.*, 2019, **12**, 1344–1356.
9 S. Kim, Y. Wang, M. S. Zhu, M. Fujitsuka and T. Majima, *Chem.–Eur. J.*, 2018, **24**, 14928–14932.
10 S. Z. Liu, Z. Guo, X. H. Qian, J. Y. Zhang, J. X. Liu and J. Lin, *Sustainable Energy Fuels*, 2019, **3**, 1048–1054.
11 F. N. Sayed, O. D. Jayakumar, R. Sasikala, R. M. Kadam, S. R. Bharadwaj, L. Kienle, U. SchÜrmann, S. Kaps, R. Adelung, J. P. Mittal and A. K. Tyagi, *J. Phys. Chem. C*, 2012, **116**, 12462–12467.
12 S. Onsuratoom, T. Puangpetch and S. Chavadej, *Chem. Eng. J.*, 2011, **173**, 667–675.
13 M. Murdoch, G. I. N. Waterhouse, M. A. Nadeem, J. B. Metson, M. A. Keane, R. F. Howe, J. Llorca and H. Idriss, *Nat. Chem.*, 2011, **3**, 489–492.
14 S. Hong, D. P. Kumar, E. H. Kim, H. Park, M. Gopannagari, D. A. Reddy and T. K. Kim, *J. Mater. Chem. A*, 2017, **5**, 20851–20859.
15 S. Zhang, X. Liu, C. Liu, S. Luo, L. Wang, T. Cai, Y. Zeng, J. Yuan, W. Dong, Y. Pei and Y. Liu, *ACS Nano*, 2018, **12**, 751–758.
16 H. Han, K. M. Kim, C. W. Lee, C. S. Lee, R. C. Pawar, J. L. Jones, Y. R. Hong, J. H. Ryu, T. Song, S. H. Kang, H. Choi and S. Mhin, *Phys. Chem. Chem. Phys.*, 2017, **19**, 28207–28215.
17 X. H. Qian, J. Y. Zhang, Z. Guo, S. Z. Liu, J. X. Liu and J. Lin, *Appl. Surf. Sci.*, 2019, **481**, 795–801.
18 D. A. Reddy, H. Park, S. Hong, D. P. Kumar and T. K. Kim, *J. Mater. Chem. A*, 2017, **5**, 6981–6991.
19 Y. Lu, D. Chu, M. Zhu, Y. Du and P. Yang, *Phys. Chem. Chem. Phys.*, 2015, **17**, 17355–17361.
20 J. Y. Zhao, X. M. Yan, N. Zhao, X. Li, B. Lu, X. H. Zhang and H. T. Yu, *RSC Adv.*, 2020, **10**, 32652–32661.
21 Z. Sun, Q. Yue, J. Li, J. Xu, H. Zheng and P. Du, *J. Mater. Chem. A*, 2015, **3**, 10243–10247.
22 K. H. Sun, J. Shen, Y. T. Yang, H. Tang and C. S. Lei, *Appl. Surf. Sci.*, 2020, **505**, 144042.
23 J. G. Yu, Y. Hai and B. Cheng, *J. Phys. Chem. C*, 2011, **115**, 4953–4958.
24 J. R. Ran, J. G. Yu and M. Jaroniec, *Green Chem.*, 2011, **13**, 2708–2713.
25 S. S. Li, D. S. Dai, L. Ge, Y. Q. Gao, C. C. Han and N. Xiao, *Dalton Trans.*, 2017, **46**, 10620–10629.
26 R. Y. Cao, H. C. Yang, S. W. Zhang and X. J. Xu, *Appl. Catal., B*, 2019, **258**, 117997.
27 X. A. Zhou, J. Jin, X. J. Zhu, J. Huang, J. G. Yu, W. Y. Wong and W. K. Wong, *J. Mater. Chem. A*, 2016, **4**, 5282–5287.
28 J. G. Yu, S. H. Wang, B. Cheng, Z. Lin and F. Huang, *Catal. Sci. Technol.*, 2013, **3**, 1782–1789.
29 L. R. Nagappagari, S. Samanta, N. Sharma, V. R. Battula and K. Kailasam, *Sustainable Energy Fuels*, 2020, **4**, 750–759.
30 X. Gou, F. Cheng, Y. Shi, L. Zhang and P. Shen, *J. Am. Chem. Soc.*, 2006, **128**, 7222–7229.
31 Z. Z. Zhang, L. Huang, J. J. Zhang, F. J. Wang, Y. Y. Xie, X. T. Shang, Y. Y. Gu, H. B. Zhao and X. X. Wang, *Appl. Catal., B*, 2018, **233**, 112–119.
32 M. H. Xiong, B. Chai, J. T. Yan, G. Z. Fan and G. S. Song, *Appl. Surf. Sci.*, 2020, **514**, 145965.
33 J. G. Hou, C. Yang, H. J. Cheng, Z. Wang, S. Q. Jiao and H. M. Zhu, *Phys. Chem. Chem. Phys.*, 2013, **15**, 15660–15668.
34 C. Liu, B. Chai, C. L. Wang, J. T. Yan and Z. D. Ren, *Int. J. Hydrogen Energy*, 2018, **43**, 6977–6986.
35 J. Y. Liu, W. J. Fang, Z. D. Wei and Z. Qin, *Catal. Sci. Technol.*, 2018, **8**, 1375–1382.
36 Z. P. Yan, X. X. Yu, A. Han, P. Xu and P. W. Du, *J. Phys. Chem. C*, 2014, **118**, 22896–22903.
37 Q. W. Liu, M. D. Wang, Y. S. He, X. X. Wang and W. Y. Su, *Nanoscale*, 2018, **10**, 19100–19106.
38 S. Wang, B. Y. Guan, Y. Lu and X. W. Lou, *J. Am. Chem. Soc.*, 2017, **139**, 17305–17308.
39 B. Qiu, Q. Zhu, M. Du, L. Fan, M. Xing and J. Zhang, *Angew. Chem., Int. Ed.*, 2017, **56**, 2684–2688.
40 L. L. Bi, D. D. Meng, Q. J. Bu, Y. H. Lin, D. J. Wang and T. F. Xie, *Phys. Chem. Chem. Phys.*, 2016, **18**, 31534–31541.
41 A. J. Bard, R. Parsons and J. Jordan, *Standard Potentials in Aqueous Solution*, Routledge, New York, 1985.
42 M. S. Nasir, G. R. Yang, L. Ayub, S. L. Wang and W. Yan, *Appl. Surf. Sci.*, 2020, **519**, 146208.